Interannual variability in warm water volume transports in the equatorial Pacific during 1993–1999

Christopher S. Meinen

Joint Institute for the Study of the Atmosphere and Ocean, University of Washington

Michael J. McPhaden

NOAA/Pacific Marine Environmental Laboratory, Seattle, Washington

Abstract

Previous studies have indicated that the volume of warm water (WWV) in the equatorial Pacific is intrinsically related to the dynamics of the El Niño–Southern Oscillation (ENSO) cycle. A gridded subsurface temperature data set, which incorporates temperature measurements from expendable bathythermograph profiles as well as measurements from the moorings in the Tropical Atmosphere and Ocean (TAO) Array, was used along with historical hydrography to quantify the variability of the WWV (with temperatures greater than $20°C$) within the region $8°S$–$8°N$, $156°E$–$95°W$ during 1993–1999. These data were also used to estimate geostrophic transports of warm water relative to a level of no motion at 1000 dbar (1 dbar = 10^4 Pa). Ekman transports were estimated using wind data from gridded observations, assimilating model output, and satellite scatterometer measurements. The results indicate that the buildup of WWV between the weak 1994–1995 El Niño event and the onset of the strong 1997–1998 El Niño event resulted primarily from an anomalous decrease in the net southward transport (geostrophic plus Ekman) across $8°S$ in the western and central Pacific. Afterwards, beginning in April 1997, WWV in the equatorial region was reduced by about 26% coincident with the 1997–1998 El Niño. Approximately half of the warm water lost during this period is accounted for by poleward transport across a wide range of longitudes, while the remaining half is accounted for by vertical water mass transformations. The implications of our results for understanding and modeling the ENSO cycle are discussed.

1. Introduction

The El Niño–Southern Oscillation (ENSO) cycle is characterized by large scale three dimensional changes in the distribution of upper ocean heat and mass in the tropical Pacific. The mechanisms responsible for these upper ocean changes, and how they modulate ocean-atmosphere interactions, have been a theme of ENSO research since Bjerknes' [1966, 1969] work over 30 years ago. Wyrtki [1975] emphasized the importance of ocean dynamics, and suggested that a build up in warm water in the western equatorial Pacific was a necessary precondition to the development of El Niño (i.e. ENSO warm events). This concept was expanded upon in Wyrtki [1985] and Cane et al. [1986] in which it was hypothesized that a build up in warm water volume (WWV) in the entire equatorial band was a precondition to El Niño. According to this hypothesis, warm water is flushed to higher latitudes during El Niño, after which the WWV slowly builds up again in the tropics before another El Niño occurs.

Aspects of WWV changes during the ENSO cycle have been examined using sea–level measurements [*Wyrtki*, 1985], expendable bathythermograph (XBT) surveys [*Donguy et al.*, 1989; *Picaut and Tournier*, 1991], or dynamical models [*Zebiak*, 1989; *Springer et al.*, 1990; *Brady*, 1994; *Brady and Gent*, 1994]. Recently Jin [1997a,1997b] and Jin and An [1999] produced a theoretical "recharge oscillator" to describe how WWV could control the timing of El Niño and La Niña events. Meinen and McPhaden [1999] used *in situ* measurements of subsurface temperature to confirm that variations in WWV over the time period 1980–1999 were consistent with Jin's hypothesized oscillator, but they did not discuss the pathways through which the warm water moved. To date there has not been a thorough study using ocean observations for the purpose of quantifying the exchange of warm water between the equatorial region

and the higher latitudes on ENSO time scales. The focus of this paper is to document the pathways through which the warm water moves during the ENSO cycle, both within the equatorial Pacific and as the warm water is exchanged with the higher latitudes.

A gridded subsurface temperature data set for the interval spanning 1980 to the present has been developed by Dr. Neville Smith and others at the Australian Bureau of Meteorology Research Centre (BMRC) [*Smith*, 1995a; *Smith*, 1995b]. This data set combines XBT data with temperature measurements from moorings. The Tropical Atmosphere and Ocean (TAO) Array [*McPhaden et al.*, 1998], which was largely in place by early 1993 and was fully deployed by December 1994, greatly increased the amount of subsurface temperature data available for the development of the BMRC gridded data set between 8°S and 8°N. Geostrophic transports can be calculated using gridded BMRC temperature measurements in combination with historical hydrography, and Ekman transports can be estimated using observational and model–based wind products. This provides the opportunity to study the movement of warm water and how that movement relates to volume changes in the region.

Warm water is defined for the purpose of this paper as water with an *in situ* temperature greater than or equal to 20°C. We concentrate on the period 1993–1999 encompassing El Niño events in 1993, 1994–1995, and 1997–1998, the latter of which by some measures is the strongest event on record [*McPhaden*, 1999]. This period also encompasses two La Niña events in 1995–1996 and 1998–1999.

The remainder of the paper is organized as follows. Section 2 presents a brief description of the data used in this study. Section 3 illustrates the methods for calculating the WWV, as well as the geostrophic and Ekman velocities and transports. The calculated transports are shown in Section 4, with a discussion of these results.

Finally a summary of the key results is presented in Section 5. Most of our discussion will focus on ENSO variations between 1994–1999 since the 1993 El Niño was rather weak and short lived, and antecedent conditions in 1991-1992 were less well sampled and thus were not included in our records.

2. Data

Subsurface temperature measurements were provided by the gridded temperature fields made available by Dr. Neville Smith of the Bureau of Meteorology Research Centre (BMRC), Australia [*Smith*, 1995a; *Smith*, 1995b]. The BMRC data set combines XBT data with data from moorings, where available, to create a gridded data set with monthly values at every 1° of latitude and every 2° of longitude at a set of 14 depths between the surface and 500 m. Since about 1993, roughly three quarters of the subsurface temperature information in the BMRC data analysis between 5°S and 5°N derives from the TAO Array [*Smith and Meyers*, 1996]. The TAO array consists of about 70 ATLAS (Autonomous Temperature Line Acquisition System) moorings and current meter moorings (Figure 1) spanning the equatorial Pacific from 137°E to 95°W $\boxed{\text{Figure 1}}$ and from 8°S to 8°N [*McPhaden et al.*, 1998]. The ATLAS moorings measure subsurface temperature at 10 depths in the upper 500 m as well as sea–surface temperature (SST), wind speed and direction. Current meter moorings generally also measure winds and ocean temperatures in addition to ocean velocities in the upper 300 m.

The lower panel of Fig. 1 shows the locations of about 3000 CTD profiles from the Pacific Marine Environmental Laboratory's database. All of the CTDs were taken during 1990–1998 and they all reach at least 1000 dbar. These CTDs were used to relate the gridded BMRC temperatures to the corresponding dynamic heights based on

empirical relationships identified in the hydrography.

Three different wind products were used in this study. The FSU wind data set, which combines measurements from ships and buoys, provides monthly wind pseudostress on a 2° by 2° grid. These data are provided by Dr. J. J. O'Brien and Dr. D. M. Legler at Florida State University via their web site. A second wind data set was obtained from the European Centre for Medium–Range Weather Forecasts (ECMWF). The ECMWF winds are on a 2.5° by 2.5° grid and are derived from an atmospheric general circulation model which assimilates measurements from many data sources including ship and TAO buoy winds. We processed twice daily ECMWF analyses to monthly means for this study. A third wind data set was obtained from the blended scatterometer measurements from the ERS–1, ERS–2 and NSCAT satellites (henceforth referred to as SCAT). The SCAT measurements were blended into a weekly data set on a 1° by 1° grid distributed by the Institut Français de Recherche pour l'Exploitation de la Mer (IFREMER) (web site: http://www.ifremer.fr/cersat/). From these weekly data we produced monthly mean winds. ECMWF and SCAT wind velocities were converted into wind stress using a constant drag coefficient of 1.43×10^{-3} and an air density of 1.225 kg m^{-3} [*Weisberg and Wang*, 1997]. The FSU pseudostress was converted to stress using a drag coefficient of 1.20×10^{-3} [*Sirven et al.*, 1998] because the larger drag produced stresses that resulted in unusually large Ekman transports in comparison to the other data sets.

Finally, we used the Reynolds SST analysis which represents a blending of satellite–based and *in situ* SST measurements [*Reynolds*, 1988; *Reynolds and Marsico*, 1993; *Reynolds and Smith*, 1994; *Reynolds and Smith*, 1995]. These SST data are on a 1° by 1° grid at weekly time–intervals. We calculated monthly averages for comparison

with the other data sets.

In order to focus on interannual variability, seasonal variations have been removed from all time series shown in this paper as follows. The mean seasonal cycle over 1993–1996 was determined and the difference between this seasonal cycle and the annual mean over 1993–1996 was defined to be the seasonal correction. The years 1997–1999 were not used in developing the seasonal correction to avoid biasing any of the large 1997–1998 El Niño into the seasonal signal. The resulting seasonal variations were removed from all of the complete time series. Comparison with a subsurface temperature seasonal correction developed using the full 19 years of the BMRC data set indicated that the subsurface temperature seasonal correction determined from the shorter time interval was representative of longer records. Seasonal corrections for winds and SST over decade–long time intervals also compared favorably with the seasonal corrections derived over the four years 1993–1996. All seasonally corrected time series have further been smoothed by a five–month running mean to remove shorter period variability.

3. Methods

We shall focus on the region defined by 8°S–8°N, 156°E–95°W, and contained between the ocean surface and the 20°C isotherm surface. The lateral boundaries were chosen to maximize the fraction of the equatorial Pacific covered while staying within the region where the most data was available for incorporation into the BMRC gridding system. The poleward–most TAO mooring lines are at 8°S and 8°N, so these lines were chosen for the meridional boundaries. The easternmost TAO line is at 95°W, giving our eastern boundary. While there is some data provided by TAO moorings west of 156°E, there are many gaps in the time series due to mooring and data losses associated with

commercial fishing activities. Thus our western boundary was chosen to be 156°E. This region spans the majority of the equatorial Pacific; the surface area of the regions west and east of our area are far smaller than the region we cover. Other lateral boundaries were tested, and the results are not particularly sensitive to the boundaries we have used. The 20°C isotherm was chosen as the base of our region because that isotherm is generally found near the center of the main thermocline in this area [*Kessler*, 1990]. Other isothermal surfaces were tested and our results were also not sensitive to the isotherm chosen as long as it was near the center of the main thermocline.

The subsurface BMRC gridded temperature measurements provide two quantities needed for this study. The depth of the 20°C isotherm, Z_{20}, was determined by interpolating between the two grid levels bounding 20°C. The heat content above 500 m, denoted by Q_{500}, was determined via

$$Q_{500} = \int_0^{500} \rho C_p T dz \tag{1}$$

where ρ, C_p, and T denote density, specific heat content, and temperature respectively. For this calculation constant values of $\rho = 1030$ kg m^{-3} and $C_p = 3995$ J kg^{-1} °C^{-1} were used. Time series of Z_{20} were integrated horizontally to determine the WWV within the dashed region in Fig. 1, while the time series of Q_{500} provided input to the geostrophic velocity calculation.

In order to determine geostrophic velocity from the gridded temperature data, the dynamic height anomalies, ΔD, that are associated with the measured temperatures need to be determined. Since the BMRC data set does not provide salinity, and the TAO buoys generally have not been instrumented to measure subsurface salinities except for special programs like TOGA–COARE [*Cronin and McPhaden*, 1998], it

is not possible to directly calculate the specific volume anomaly, δ, at each depth during our study interval. Instead, a method for using temperature–salinity (T–S) characteristics determined from historical hydrography is needed. Two methods were tested for obtaining the ΔD: Using a T–S relationship developed for each TAO mooring site [*Johnson and McPhaden*, 1999]; and using the integrated Q_{500} to characterize the vertical profile of δ after Meinen and Watts [2000]. Meinen and Watts [2000] demonstrated that in the Newfoundland Basin an integral measure of the heat content, in that case round trip acoustic travel time, was able to provide a robust estimate of the corresponding vertical profile of specific volume anomaly when combined with historical hydrography from the region. This method produced better results in our final volume budget than using the more traditional mean T–S approach, and thus was adopted for all results shown in this paper.

A basic review of the $T \rightarrow \Delta D$ methodology, and a discussion of the application of this technique to the equatorial Pacific, is provided here. The roughly 3000 CTD profiles reaching at least 1000 dbar during the 1990–1998 interval (Fig. 1) were separated into overlapping latitude subsets 4° wide and spanning the basin between 128°E and the coast of the Americas. Next, each CTD cast was used to calculate a value of Q_{500} via Eqn. 1. Finally, the δ values calculated with each of the CTD casts within a latitude subset are smoothed onto a regular grid of pressure and Q_{500}. As an example of the structural variations captured by these smoothed grids, the gridded δ values developed using hydrography within 6°N–10°N (Figure 2, upper panel) show the shoaling of

Figure 2

the pycnocline at progressively lower values of Q_{500}. This shoaling appears to be the dominant variation in the vertical structure in this latitude band. The variation of the vertical structure shown in Fig. 2 is referred to as the variation of the "Gravest

Empirical Mode" or GEM.

One feature of this GEM technique is that the smoothed grid of δ values can be compared against the original δ values calculated from the CTD profiles to determine just how well the historical hydrographic data can be characterized by the integrated Q_{500} values. The RMS (root–mean–square) difference between the δ values directly calculated from the CTD data and the δ values from the smoothed field was determined within bins of 50 dbar by 5×10^8 J m^{-2} (Fig. 2, lower panel). The scatter about the smoothed field is fairly small compared to the observed signal, generally 5–15%. This scatter represents a natural error bar for the GEM smoothed δ values.

The smoothed grid of δ in Fig. 2 is used to obtain a time series of δ profiles using the time series of measured Q_{500} from the gridded BMRC temperature data along the meridional TAO mooring lines at 8°N. The GEM technique is repeated at each 1° of latitude on each meridional line of TAO moorings, with a latitude subset of CTDs centered on each latitude used to develop the associated GEM field. The result is δ profile time series at each 1° of latitude along each meridional line of TAO moorings. The technique presented here is essentially the same as the technique described in Meinen and Watts [2000] except that where that study used the simulated acoustic round trip travel time to characterize the vertical structure this study uses Q_{500}. Also the Meinen and Watts [2000] study centered in a smaller region, the western Newfoundland Basin, and could use a single GEM field while this study focuses on a much larger and more complicated region best split into latitudinal subsets to characterize the observed changes in vertical structure and water masses.

Along each of the meridional lines of TAO moorings at 1° meridional resolution the appropriate smoothed GEM field was used to produce time series of δ profiles from

the surface to 1000 dbar. These δ profiles are then integrated vertically to give profiles of ΔD. Finally, using the dynamic method [*Pond and Pickard*, 1983], profiles of ΔD from adjacent sites can be used to determine the normal component of the geostrophic velocity relative to 1000 dbar. This calculation was made poleward of 1°N and 1°S where previous studies have indicated that the geostrophic approximation was good [*Kessler and Taft*, 1987; *Picaut and Tournier*, 1991]. The zonal component of the velocity on the equator was estimated using the meridionally differentiated form of the geostrophic approximation

$$\beta u = -\frac{\partial^2 \Delta D}{\partial y^2} \tag{2}$$

where β, u, and ΔD represent the meridional derivative of the Coriolis parameter, zonal velocity, and dynamic height anomaly respectively [*Bryden and Brady*, 1985; *Picaut et al.*, 1989; *Picaut and Tournier*, 1991]. Picaut et al. [1989] compared the results from applying this second derivative method to the TAO buoys at 2°S, 0°N, and 2°N (which is mathematically the same as averaging two geostrophic estimates determined via the standard dynamic method between 0°N–2°N and 2°S–0°N) to direct current meter measurements on the equator at 165°E and 110°W. Their results indicated that the interannual variability of the zonal currents was well estimated using Eqn. 2.

The net transport in the ocean consists of both geostrophic and Ekman components. Ekman transports were calculated for this region using ECMWF, FSU, and SCAT wind products. These transports were calculated poleward of 2°S and 2°N using the drag coefficients and air densities listed earlier in the Data section and the standard technique for evaluating Ekman transports [*Pond and Pickard*, 1983]. The zonal Ekman transport between 2°S and 2°N was neglected; it will be shown later that this omission is not a serious limitation.

4. Results

The mean, standard deviation (STD), and empirical orthogonal functions (EOFs) [*Emery and Thomson*, 1997] of Z_{20} were calculated (Figure 3). The basic Z_{20} structure in this region details a shoaling thermocline to the east with the largest interannual variability occurring along the equator in the eastern Pacific. The first two EOF modes, explaining 45% and 35% of the total variance respectively, represent an "east–west tilting" mode pivoting around 150°W and an equatorial "recharge–discharge" mode pivoting along a nodal line roughly coinciding with the North Equatorial Counter– Current (NECC) pathway. The equatorial recharge–discharge mode preceded the east–west tilting mode by about seven months (Fig. 3, bottom panel), consistent with the theoretical recharge–discharge oscillator of Jin [1997a]. Higher EOF modes each explained less than 7% of the total variance.

Based on the observed changes in Z_{20} it is apparent that the volume of water warmer than 20°C in this region must change significantly over time (Figure 4). The timing of the WWV anomalies generally leads by about seven months changes in the anomalous sea–surface temperature (SST) spatially averaged over the NINO3 region, bounded by 5°S to 5°N, 150°W to 90°W (Fig. 4) [*Meinen and McPhaden*, 2000]. The NINO3 SST is one of many commonly used indicators of the current phase of the ENSO oscillation [*Trenberth*, 1997], with peaks in December 1994 and November 1997 indicating the peak of the 1994–1995 and 1997–1998 El Niño events. The buildup of warm water in the tropics prior to El Niño events hypothesized by Wyrtki [1985] on the basis of sea–level measurements is confirmed both for the 1994–1995 El Niño and for the 1997–1998 El Niño. The buildup in both cases is not abrupt, but rather takes place slowly. The buildup before the 1997–1998 El Niño takes place over more than a

Figure 3

Figure 4

year. Then, in October 1994 and again in April 1997 the volume of warm water begins to drop; during the 1997–1998 El Niño event the volume of warm water drops by about 26%. In order to document where this warm water goes as it leaves this region it is necessary to estimate the zonal and meridional transports.

4.1. Geostrophic velocities and transports

Menkes et al. [1996] used about 16 months of TAO data from 1992-1994 to demonstrate that the ΔD anomalies determined from the TAO array temperatures could produce an estimate for the anomalous geostrophic surface velocity that compared well with both the velocities determined from TOPEX/Poseidon altimetry measurements and *in situ* velocity measurements by current meters. A similar geostrophic technique was applied to our calculated ΔD profiles to determine geostrophic velocities within our study region. In contrast to Menkes et al. [1996], however, who were interested primarily in comparisons with TOPEX/Poseidon, we calculated velocities without the removal of the long term mean, and more importantly we calculated the geostrophic velocities at 10 m vertical intervals down to 1000 m rather than just at the surface.

Similar to the processing for Z_{20}, the mean, STD, and EOFs were calculated for the zonal geostrophic surface velocity (U_g) to provide information about its variability (Figure 5). The mean structure shows the large scale surface currents, the westward $\boxed{\text{Figure 5}}$ flowing South Equatorial Current (SEC) and the eastward flowing NECC. The SEC spans about 8°S–6°N in the eastern Pacific and about 8°S–0°N in the western Pacific. There are two branches of the SEC, one north of the equator and the other south of the equator, with a minimum on the equator. The NECC is located north of the SEC. This mean structure is consistent with the mean picture obtained by Reverdin et al.

[1994] using drifting buoy and current meter records to determine the surface currents. The STD of U_g peaks just south of the transition zone from the northern branch of the SEC and the NECC. The first EOF mode, which represents 49% of the total variance, is essentially an eastward–westward reversing of U_g throughout the basin with peaks coinciding with the peaks in the STD. The second EOF mode, which represents 13% of the total variance, has alternating signs north and south of the SEC–NECC transition zone. Higher modes each represent less than 9% of the total variance.

The first EOF suggests that during the onset and mature phases of the 1994–1995 and 1997–1998 El Niño events the NECC strengthened roughly between 4°N and 8°N while the SEC weakened between 8°S and 4°N. During the demise of these El Niño events and the subsequent La Niña events the reverse occurs with a significant weakening of the NECC and strengthening of the SEC. The variations in these currents were about 3–4 times larger during 1997–1998 than 1994–1995.

To understand the overall movement of warm water east–west as well as north–south the geostrophic transport of warm water was calculated across each meridional line of TAO moorings within our region as well as across each of the zonal lines of moorings except for the line right on the equator. Figure 6 shows the geostrophic transport of warm water across 156°E, 155°W, and 95°W integrated above Z_{20} and between 8°S and 8°N. At 156°E the geostrophic transport of warm water between 8°S and 8°N was always eastward with increases of 15–25 Sv (1 Sv = 10^6 m^3 s^{-1}) during the 1994–1995 and 1997–1998 El Niño events, and a decrease to near zero transport in mid–1998. At 155°W and 95°W the geostrophic transport of warm water was generally westward except during the onset and mature El Niño phases as defined by NINO3. During those periods, the zonal transports reverse and become eastward or, in the case of

| Figure 6 |

the 1994–1995 El Niño, decrease to zero. The magnitudes of the east–west transport variations in 1994–1995 were consistently weaker than those during 1997–1998.

The geostrophic transports of warm water across 8°S and 8°N were integrated above Z_{20} and between 156°E and 95°W (Figure 7). Meridional geostrophic transports are generally equatorward since the zonal pressure gradient is generally negative (i.e. deeper thermocline in the west). However, during the El Niño events a decrease in the equatorward flow was noted both north and south of the equator, and in late 1997 and early 1998 the equatorward flow went to zero. These variations are consistent with the reduction of the trade winds and the flattening of the zonal tilt of the main thermocline between 8°S and 8°N during El Niño.

Figure 7

4.2. Ekman transports

The three different wind products discussed previously in the Data section were used to calculate Ekman transports along each meridional and zonal line of the TAO array. Ekman transports were considered to be wholly of warm water ($T \geq 20°C$), assuming that the depth of the Ekman layer was shallower than Z_{20}, which ranges between 50–200 m. While this assumption may be suspect at times, the expected decrease in Ekman velocity with depth assures that most of the resulting Ekman transport occurs in the near surface waters. As the Ekman relation fails near the equator where the Coriolis parameter goes to zero, Ekman transports were calculated only poleward of 2°S and 2°N. Neglect of wind–driven frictional zonal currents equatorward of 2° does not adversely affect our calculations since these flows are very shallow and weak with very small transports relative to the geostrophic currents [*McPhaden*, 1981; *Picaut et al.*, 1989]. The zonal Ekman transports across 156°E, 155°W, and 95°W

(not shown) were only 1–3 Sv, an order of magnitude smaller than the corresponding zonal geostrophic transports, regardless of which wind product was used.

Meridional Ekman transports across 8°S and 8°N (Figure 8), which peak around 30 Sv, were much larger than zonal Ekman transports. The variability of these meridional transports is comparable in magnitude to the variability of the meridional geostrophic transports, with peak–to–peak changes around 10–15 Sv at 8°N and about 15–20 Sv at 8°S. Differences resulting from wind products are also apparent in the meridional Ekman transports. In particular, the ECMWF and FSU wind products agreed with each other better over most of this time interval than with the SCAT winds, which tended to be more variable.

During the weak La Niña event in 1995–1996 all three products indicate a gradual peaking in the poleward Ekman transport across both 8°S and 8°N. Then, just prior to the 1997–1998 El Niño, the poleward Ekman transports began to decrease across both 8°S and 8°N, consistent with the slackening trade winds. The meridional Ekman transports never reduced to zero during the 1997–1998 El Niño event, unlike the meridional geostrophic transports, and by mid–1998 the Ekman transports returned to the pre-El Niño values.

4.3. Net horizontal transports

Based on island–based sea–level measurements, Wyrtki [1985] suggested that El Niño is preceded by a buildup of warm water in the equatorial band, followed by a flushing of warm water poleward out of the equatorial Pacific. Consistent with this hypothesis, the time series of WWV shown earlier (Fig. 4) indicates a build up prior to and significant decrease during El Niño. Net transports (Ekman plus geostrophic)

Figure 8

across 8°S and 8°N (Figure 9) show that during El Niño the transport of warm water to higher latitudes increased. (For simplicity in this section the ECMWF winds will be used for the Ekman transport computations, though the essential results presented are not sensitive to the wind product used. The ECMWF winds are chosen for illustrative purposes because they consistently compared well with one or both of the other products.) By comparing the geostrophic and Ekman transport components it can be observed that the transport of warm water to higher latitudes was primarily due to a decrease in the equatorward geostrophic transports, not due to an increase in the poleward Ekman transports. This is most obvious during the 1997–1998 El Niño, when the equatorward geostrophic transports approached zero in late 1997 and early 1998 (Fig. 7) while the poleward Ekman transports (Fig. 8) remained non–zero and thus continued to transport warm water to higher latitudes. These tendencies are also visible during the weaker 1994–1995 El Niño event, and are consistent with the modeling results of Pares–Sierra et al. [1985], who used a linear numerical model forced by observed winds for the period 1962-1979.

The buildup of warm water in the equatorial region (Fig. 4) prior to the 1997–1998 El Niño began in October 1995, during the 1995–1996 La Niña, and continued until March 1997. During this time the net transport across 8°N was fairly constant, at about 13 Sv to the north, which is near the long term mean. The net zonal transports across 156°E and 95°W (Figure 10) at the same time were increasing slightly. The anomalous zonal transport across the two lines, however, nearly matched throughout most of the time series, with the exception of mid–to–late 1997 when the anomalous flow eastward across 156°E was about 10 Sv larger than the anomalous eastward flow across 95°W. There was a significant anomalous weakening of southward transport across 8°S prior

| Figure 9 |

| Figure 10 |

to the 1997–1998 El Niño, such–that the absolute net transport across 8°S was close to zero or weakly northward during this time (Fig. 9). So most of the warm water added to the equatorial region prior to the 1997–1998 El Niño came from the west as part of the long-term mean zonal convergence (upper panel, Fig. 10), coupled with an anomalous decrease in the southward flow across 8°S.

In April 1997 the WWV began to drop quickly as the 1997–1998 El Niño event developed. Across 8°N a net poleward transport increase began in March–April 1997 and continued until December 1997. Across 8°S the southward transport (negative values in Fig. 9) began to increase in February–March 1997 and continued, with a break between November 1997 and March 1998, until June–July 1998. There was an obvious El Niño related signal in the zonal net transports (Fig. 10), and the anomalous transport across 95°W was smaller than the anomalous transport across 156°E in mid–to–late 1997. Thus while the meridional transports were divergent, discharging warm water during 1997 and early 1998, the zonal transports were anomalously convergent, bringing additional warm water into the region. The meridional divergence was larger than the zonal convergence, which resulted in a decrease in WWV. After the 1997–1998 El Niño, WWV again began to build up, primarily due to reduced southward transport across 8°S.

Regarding the WWV changes during the 1994–1995 El Niño event, the poleward transports across 8°S and 8°N began to increase in June and September 1994, respectively, resulting in enhanced meridional divergence. These increases in poleward transports occurred several months later in the calendar year during the 1994–1995 El Niño than during the 1997–1998 El Niño, which may be related to the fact that the events were phased differently relative to the seasonal cycle. During the WWV

buildup prior to the 1994–1995 El Niño, zonal transport anomalies across 156°E and 95°W indicated a small zonal divergence, and the anomalous reduction in the southward transport across 8°S occurred during only a short period in early 1994 just a few months before the peak SST.

To determine where within the basin the poleward transports were taking place, the meridional net (Ekman + geostrophic) transport was calculated as a function of longitude and time across 8°N (Figure 11) and 8°S (Figure 12). The units of these transports are Sv °Lon^{-1}, representing meridional transport per degree of longitude along the zonal line at 8°N or 8°S. During much of the 1993–1996 time frame the anomalous transports (Figs. 11 and 12, right panels) were near zero. During September 1994–March 1995 there was anomalous southward transport across 8°N between the dateline and 160°W, partially offset by poleward flow further to the east. On the other hand, during June 1994 through June 1995 there was increased southward flow across 8°S west of 160°W, which was large enough to dominate the overall meridional volume divergence during this time period. These were the only signals of significance during the weak 1994–1995 El Niño. Between October 1995 and March 1997, during the buildup of warm water in the equatorial region (Fig. 4), the anomalous transport of warm water towards the equator appears to occur preferentially west of 155°W across 8°S. There is little indication of anomalous flow across 8°N during this period.

During the strong 1997–1998 El Niño there was increased northward transport across 8°N throughout much of the basin beginning in August 1997 and continuing through September 1998. Beginning in May–June 1997 there was increased anomalous southward transport across 8°S spanning from 170°E to 95°W with the strongest anomalies centered near 170°W. Subsequently during the 1998–1999 La Niña, strong

Figure 11

Figure 12

equatorward transport anomalies appeared in late 1998 and early 1999, again primarily confined to the west of 155°W at both 8°S and 8°N. This meridional discharge and recharge of WWV during and after the El Niño event is consistent with the sea level measurements of Wyrtki [1985], although the distribution of the warm water discharge throughout the basin is inconsistent with Wyrtki's hypothesis of the strongest poleward flows occurring along the coast of the Americas.

4.4. Volume balance

Seawater is nearly incompressible, so changes in WWV within the dashed region in Fig. 1 should balance the volume transports of water across the boundaries of the region. The flow across the boundaries includes the Ekman and geostrophic transports mentioned earlier as well as volume transports across the ocean surface (precipitation minus evaporation) and across the 20°C isotherm. We can use observations to estimate precipitation minus evaporation $(P - E)$, but it is not possible to directly measure the volume transport across the 20°C isotherm. This latter transport will therefore be computed as a residual of the volume balance.

An estimate of the transport of water at the ocean surface was determined from the climatological $P - E$ provided as part of the da Silva et al. [1994] atlas of surface marine data. Integrating the annual mean $P - E$ over our region gives a sea–surface volume transport of about 0.05 Sv. Rainfall is difficult to measure over the ocean, however even if this estimate is an order of magnitude too small the input through the ocean surface is still negligible with regards to the total volume balance. Because this transport is so small, $P - E$ is neglected in our volume budget.

The volume transport across the 20°C isotherm is related to, but distinct from,

kinematic vertical velocities. Cross–isothermal transports are associated with diathermal mixing and water mass transformations, and represent that part of upwelling and downwelling velocities that are linked to vertical heat fluxes [*Bryden and Brady*, 1985]. For example, upward volume transport across the 20°C isotherm implies a cooling tendency in the upper ocean which would be partially balanced by surface heating, as occurs during periods when the cold tongue is well developed in the eastern Pacific. On the other hand, a downward volume transport across the 20°C isotherm implies a loss of heat from the upper ocean, as would occur in the eastern Pacific during El Niño events when surface fluxes anomalously cool the upper ocean (e.g. Sun and Trenberth [1998], Wang and McPhaden [2000]).

The changes in the warm water volume within our region can be compared to the total net transports into and out of the region across the lateral boundaries (Figure 13; Tables 1–3). This comparison was made separately using the Ekman transports from all three wind data sets. The geostrophic transports used in each comparison were the same, as were the observed warm water volume changes. The mean circulation pattern for this region was characterized by zonal convergence and meridional divergence (Tables 1&2). On average warm water entered from the west at 156°E and the east at 95°W, with the resulting excess flowing towards the poles. Generally the net poleward flow to the north across 8°N was about twice as strong as the flow to the south across 8°S.

The difference between the mean WWV change within the box and the mean net transport across the sides of the box represents an estimate for the mean vertical transport across 20°C within our region. Using FSU, ECMWF, and SCAT winds for the Ekman components yields mean vertical transport estimates of -3, 0, and 0 Sv,

| Figure 13 |

| Tables 1&2 |

respectively (Table 3). Based on the uncertainties in the net transports through the sides [Table 3] of the box (see Appendix) we estimate a standard error of 6 Sv for the mean vertical transport estimate. Thus, for the period January 1993–May 1999, the temporally averaged cross–isotherm vertical volume transport spatially integrated over 8°S–8°N, 156°E–95°W was not statistically different from zero.

Variations in the total transport into the region were significantly correlated at the 95% level of confidence with the observed changes in warm water volume when the Ekman transports are computed using the ECMWF and FSU wind products, yielding correlations of 0.51 and 0.52 respectively (Table 2). The correlation was lower (0.45) when the SCAT wind product is used, though the differences between the comparisons using three wind products is of marginal statistical significance in these calculations. The differences between horizontal transport convergences and volume changes are contaminated by sampling and computational errors. The error bars estimated for the zonal and meridional volume transports, 7 Sv for the 5–month running–mean zonal transport across 156°E or 95°W and 9 Sv for the corresponding meridional transports across 8°S or 8°N (derived in the Appendix), are comparable to the RMS differences between the transports and the volume changes (Table 3). However, at least part of the differences between the volume changes and the horizontal transport convergences may be related to variations in cross–isothermal transports, as discussed next.

During the 1997–1998 El Niño event there was a consistent trend for the horizontal transports into the box to be larger than observed warm water volume changes can explain, regardless of which wind field is used. In particular, balancing the volume budget for the period from March 1997 to about March 1998 would require a mean downward transport of about 14 Sv across the 20°C isotherm (plus or minus a few Sv

depending on which wind product is used). During March 1998 through early 1999, on the other hand, balancing the volume budget would require a mean upward transport of about 10 Sv across the 20°C isotherm. These large cross–isotherm transports demonstrate that vertical exchange plays an important role in the WWV budget.

The 1997–1998 El Niño event also can be used to illustrate the relationships between the magnitudes of the various components of the volume balance. While warm water was being discharged from the equatorial region during April 1997 through July 1998 (Fig. 4), the temporal mean meridional and vertical divergences averaged about 10 Sv and 12 Sv respectively (depending on which wind product was used for the Ekman component these values varied by about $\pm$ 3 Sv). During the same interval the zonal flows were convergent at about 4 Sv (regardless of which wind product was used). This indicates that about equal amounts of warm water was lost meridionally, towards the poles across 8°S and 8°N, and vertically, through water mass conversion at the 20°C isotherm, while the zonal convergence played a smaller role in the volume balance. These qualitative relationships between terms also seem to hold during the much smaller 1994–1995 El Niño event with the meridional and vertical divergences playing the nearly equal roles in the WWV changes, and the zonal component playing a lesser role.

The vertical transports discussed above are averaged over the entire region outlined in Fig. 1, although it is expected that the majority of these transports occurred close to the equator where vertical mixing processes are particularly vigorous. We would also expect there to be significant zonal asymmetries in vertical volume transports given the zonal asymmetries in the Z_{20} variations (Fig. 3). These asymmetries are discussed further in the next section.

4.5. Eastern and western basin volume budgets

Surface currents (Fig. 5) and zonal transport time series (Fig. 10) show that warm water was not only exchanged between the equatorial region and the higher latitudes, but also between the eastern and western parts of the equatorial Pacific. The EOFs of Z_{20} (Fig. 3) also show significant zonal asymmetries in the vertical excursions of the thermocline. To examine the distinctive variations that occur in the eastern and western halves of our region, we separate the WWV shown in Fig. 4 into the volume west of 155°W, V_w, and the volume east of that longitude, V_e (Figure 14, upper panel). The choice of 155°W was made as it was near the zero line in the first EOF of Z_{20}.

$\boxed{\text{Figure 14}}$

We find that V_w and V_e tend to vary out of phase, with the peak correlation occurring for V_w leading V_e by about 8 months (Fig. 14, upper panel). For example, the buildup of V_w prior to the 1997–1998 El Niño was followed in late 1997 by a large accumulation of warm water in the eastern Pacific. These variations imply large scale east–west redistributions of warm water that are ultimately related to low frequency equatorial Rossby and Kelvin wave dynamics [*Battisti*, 1988; *Schopf and Suarez*, 1988; *Boulanger and Menkes*, 1999].

The volume balance analysis of the previous section was repeated for the western and eastern halves of our region to quantify the extent to which zonal convergences, meridional convergences, and cross–isothermal transports affect V_w and V_e (Fig. 14, middle and lower panels). In the western equatorial Pacific the changes in V_w were well correlated with the zonal convergences, and less so with the meridional convergences. The zonal and meridional convergences had little correlation with each other, though on average they are of opposite sign (zonal convergence and meridional divergence). In the eastern equatorial Pacific variations in zonal convergence dominated those in meridional

convergence. This is consistent with the variability in meridional transports discussed earlier (Figs. 11 and 12), which indicated a marked decrease in meridional transport variability in the eastern Pacific as compared to the western Pacific.

The differences between the observed V_w and V_e changes and the net horizontal transports provide estimates for the vertical transport across the 20°C isotherm in each of the two regions (Figure 15). Interannual variations in vertical transports are negatively correlated between west and east, with the latter being of larger amplitude. Mean seasonal variations in these cross–isotherm vertical transports, which have been removed from the curves shown in Fig. 15, are roughly ± 5 Sv and are significantly smaller than the observed interannual variability. The time series mean vertical transports are 6 Sv downward and 5 Sv upward for the western and eastern subregions, respectively. These values are comparable to the estimated error bars, but consistent in sign with expectations from wind–driven circulation theory. The 5 Sv mean value for the eastern equatorial Pacific is similar in magnitude to the 7 Sv value computed by Bryden and Brady [1985] across the 23°C isotherm for roughly the same region.

Temporal variations in the estimated vertical transports were also consistent with expectations based on ENSO dynamics. In particular, in the eastern Pacific during the La Niña event of 1995–1996, 10–20 Sv were transported upward across the 20°C isotherm. This period corresponded to shallower than normal thermocline depths and stronger than normal trade winds, both of which would favor intensified upwelling and turbulent mixing. Conversely, at the height of the 1997–1998 El Niño in December 1997, when the thermocline was deep, the SST was anomalously warm, and the local winds were weak, there was a downward transport of about 20 Sv of warm water across the 20°C surface in the eastern Pacific. Subsequently during the 1998–1999 La Niña,

Figure 15

enhanced upward transport occurred at a rate of 25–30 Sv even though the zonal wind stresses in that region were anomalously weak. The depth of the thermocline was unusually shallow at that time [*McPhaden and Yu*, 1999] which facilitated enhanced mixing of heat and mass across the 20°C isotherm despite the unusually weak regional trade winds.

In the western Pacific, the three warm episodes in 1993, 1994–1995 and 1997–1998 were characterized by less downward volume transport or anomalous upward transport across the 20°C isotherm compared to the long-term mean. These were periods of anomalously weak and therefore less upwelling favorable regional winds. The intensity of cross–isotherm transport variations in this region is governed more by the vertical position of the thermocline than it is by the strength of the trade winds. The shallowness of the thermocline west of 155°W during El Niño events favors transport of thermocline water into the near surface region since wind magnitudes (regardless of the wind direction) provide a source of turbulent energy large enough to mix deeper cold waters upward.

5. Summary and Conclusions

We have used the BMRC gridded temperature data set, developed using data from XBTs and the moored TAO array, along with historical hydrography in the tropical Pacific to quantify variations in warm water volume (>20°C) in the region 8°S–8°N, 156°E–95°W, and to quantify variations in geostrophic transports within that region. Ekman transports were also estimated using FSU (gridded observations), ECMWF (model output), and SCAT (satellite scatterometer) wind products. The net transports (Ekman + geostrophic) across the boundaries were determined and were used to address

a number of issues concerning the warm water volume budget of the tropical Pacific during 1993–1999.

Measurements confirm that a significant poleward movements of warm water into and out of the equatorial Pacific occur during various phases of the ENSO cycle. For example, buildups of warm water within 8°S–8°N, 156°E–95°W prior to and after the 1997–1998 El Niño event were mainly due to the anomalous cessation or reversal of the net poleward transport across 8°S west of 155°W along with some increase in eastward flow across 156°E. During the 1997–1998 El Niño event about 26% of the warm water in this region was lost, with about half of the warm water flushed towards higher latitudes. This poleward anomalous flow across 8°S and 8°N was observed over a broad range of longitudes between 156°E and 95°W. This result is more consistent with large scale Rossby waves dynamics affecting poleward volume transports throughout the basin than it is with the discharge along the eastern boundary suggested by Wyrtki [1985].

The residual difference between the observed warm water volume changes and the net transports into the region as a whole, and into western and eastern subregions separately, provides estimates for the vertical transports across the 20°C isotherm associated with diathermal mixing and water mass conversion. During El Niño events the net horizontal transports into our region were larger than the observed warm water volume could explain, indicating transport of water downward across the 20°C isotherm. In the 1997–1998 El Niño event, which coincided with a small zonal convergence, the downward transport across 20°C constituted about half of the warm water lost while the meridional divergence constituted the other half. Because there were significant zonal asymmetries to the vertical cross–isotherm transports the volume budget was repeated for two smaller portions of our region, splitting the box at 155°W.

East of 155°W there is a downward volume transport across the 20°isotherm surface during the 1994–1995 and 1997–1998 El Niño events, coincident with decreases in zonal wind stress and increases in the depth of the thermocline. Conversely during the 1995–1996 and 1998–1999 La Niña events we observed enhanced upward volume transports. In the western half of our study region the largest vertical transport signals are increased downward transports across the 20°C surface during La Niña events, and reduced downward (or upward) transports during El Niño events. In this region, winds are actually less upwelling favorable during El Niño, but the shallower than normal thermocline creates a situation conducive to enhanced vertical turbulent transports of thermocline water into the surface layer.

Vertical volume transports described in this study are intimately linked to the heat balance of the upper ocean. In particular, anomalously large upward cross–isothermal volume transports require that there be anomalous heating of the upper ocean, whereas anomalously large downward cross–isothermal transports require anomalous cooling of the upper ocean. Qualitatively, this implies that on interannual time scales in the tropical Pacific, surface fluxes and ocean dynamical processes tend to oppose one another in terms of their effects on upper ocean heat content and ultimately SST. A complete heat balance analysis to explore these issues is beyond the scope of the present study. We are, however, pursuing a study of the heat balance, using constraints of our volume budget as essential input.

While our study region did not extend far enough to the west to observe the western boundary currents, the impact of the western boundary currents on the equatorial ocean interior is reflected by the zonal transports across 156°E. The anomalous zonal transport across 156°E was observed to oppose the WWV changes during most of

1993–1999. During the 1994–1995 and 1997–1998 El Niño events when the WWV was decreasing the eastward transport across 156°E increased, and the opposite was true during the intervening La Niña events. This increased eastward transport during El Niño events could be supplied by two sources; increased equatorward transport of warm water by the western boundary currents, or simply draining the warm water out of the region to the west of 156°E. The volume of warm water west of 156°E is approximately 5×10^{14} m^3 (assuming an area 10° latitude by 20° longitude and a 20°C depth of 200 m). The anomalous eastward transport across 156°E is roughly 10 Sv averaged over about a little over a year during the 1997–1998 El Niño event. This would drain all of the warm water volume to the west in about a year and a half. Observations at the TAO buoys west of 156°E indicate that the 20°C isotherm only shoaled by about 30 m during the 1997–1998 El Niño, so the majority of the warm water transported across 156°E must have been supplied by meridional convergence west of 156°E. The interior ocean meridional transports are typically 0.1–0.2 Sv ° Lon^{-1}. Therefore, over the approximately 10° of longitude west of 156°E but east of the western boundary currents the meridional transports would be on the order of 2 Sv from the north and south. These transports are too small to account for the observed zonal transport variability across 156°E, so the western boundary currents must be contributing the significant fraction of the anomalous transport across 156°E. This logic suggests that the western boundary currents are out of phase with WWV changes, a result predicted by Zebiak [1989] using a dynamical model.

Our results are consistent with and extend those of previous studies which used island–based sea–level measurements [*Wyrtki and Wenzel*, 1984] and dynamical models [*Pares-Sierra et al.*, 1985; *Zebiak*, 1989; *Springer et al.*, 1990]. These results provide

some new insights into mechanisms involved in warm water volume changes and movements associated with the ENSO cycle, and they characterize variability during the recent unusually strong 1997–1998 El Niño and subsequent La Niña event. As such our results can be useful for numerical model validation of simulations during the 1993–1999 time frame and for comparison with future ENSO time scale variations in the tropical Pacific.

Appendix: Accuracy of velocity, transport, and volume estimates

There are four distinct types of error which affect the estimated accuracy of the observed quantities: instrumental, methodological, spatial sampling, and temporal sampling errors. For the purpose of this Appendix the first three will be combined and are referred to as measurement error. Temporal sampling errors affect only the estimates of the time series means and are determined using the statistical standard error of the mean. The standard error of the mean is calculated in the normal manner with the number of degrees of freedom (DOF) determined using an integral time scale technique [*Emery and Thomson*, 1997]. The time series in this paper, with the seasonal cycle removed and a 5–month running–mean applied, generally contained about 10 DOF. The effect of the measurement error on the long term mean is also estimated using the observed DOF, which provides an upper bound since the decorrelation time scale for the measurement errors is likely to be no longer than that of the interannual signals being observed. The remainder of this Appendix focuses on an estimation of the measurement error for both the 5–month running–mean values and the time series mean values; error bars quoted in the text represent the total error calculated by combining the various

types of error in a square–root of the sum of the squares sense (which assumes the different sources of error are independent).

The BMRC data set includes accuracy estimates for the gridded Z_{20} values, as well as the values themselves. To determine the accuracy of the integrated WWV, a propagation of errors approach was taken [*Emery and Thomson*, 1997]. The WWV accuracy was determined as the square root of the sum of the squared errors of the gridded Z_{20} values plus the covariances between errors at neighboring grid points (since errors at adjacent points are not independent). The resulting WWV accuracy is about 0.015×10^{15} m^3 for WWV values after the application of the 5–month running–mean (which is used throughout this study), and 0.006×10^{15} m^3 for the temporal mean during the time period January 1993–May 1999.

The accuracy of the Ekman transport is difficult to quantify because the main source of error, inaccuracy in the surface wind fields, is not precisely known. This error can best be estimated by looking at the differences between the various wind products. The RMS differences between the meridional Ekman transports across 8°S and 8°N determined from the three wind products are about 7 Sv for the values after the application of the 5–month running–mean and 2 Sv for the time series mean. The zonal Ekman transports differ by about 1 Sv for the values after the application of the 5–month running–mean and 0.3 Sv for the time series mean.

Errors in the geostrophic velocities are given by

$$\epsilon_v = \sqrt{\epsilon_\Phi^2 + \epsilon_{ref}^2} \qquad (A1)$$

where $\epsilon_\Phi = \frac{\delta(\Delta D)}{fL}$ is the error due to inaccuracies in the calculated dynamical heights and ϵ_{ref} is the error in the reference velocity [*Johns et al.*, 1989]. No reliable error

estimate is available for the "reference" velocity at the assumed level of no motion of 1000 dbar. There have been a few measurements of deep velocities in this region and there is evidence that the zonal flow at 1000 dbar may be non–zero both in the mean and at interannual time scales [*Firing*, 1987; *Davis*, 1998], however further study is needed to confirm these results. Due to a lack of concurrent measurements we neglect this source of error on the assumption that it is relatively small. Thus, the measurement error for geostrophic velocities, ϵ_v, was estimated only by considering ϵ_Φ.

The largest error in determining ΔD is due to T–S variability, in this case represented by the scatter about the GEM fields. To quantify this error, each CTD in Fig. 1 was used to calculate the surface dynamic height anomaly in two ways: directly via the equations of state [*Fofonoff and Millard*, 1983]; and also by calculating Q_{500} from the measured temperatures and using the GEM technique described in the text. The RMS difference between the surface ΔD determined via the two different methods is 3.5 dyn cm, with the largest differences occurring in the western Pacific. This value is similar to earlier estimates of 3 dyn cm and 2 dyn cm for the salinity variability induced ΔD errors in the western and eastern equatorial Pacific, respectively [*Busalacchi et al.*, 1994]. At 8°N or 8°S, where $|f| = 2.0 \times 10^{-5}$ s^{-1}, an error in ΔD of 3.5 dyn cm across the span between 156°E and 95°W would lead to a velocity error of $\epsilon_\Phi \approx 1$ mm s^{-1}. This corresponds to a meridional transport error of about 0.5 Sv for the long–term mean and about 2 Sv for the 5–month running means.

Determining the zonal transport accuracy between 8°S and 8°N is more complicated due to the latitudinal variation in the Coriolis parameter. Treating the spans over 8°S–0°N and 0°N–8°N separately and using a value of f at 4°, an error in the dynamic height difference of 3.5 dyn cm across a span of 8° of latitude yields a velocity error

of 4 cm s^{-1}. Corresponding transport errors for the zonal transports integrated over 8°S–8°N would be 3 Sv for the long–term mean and 9 Sv for the 5–month running–means. These values may exaggerate the error, however, because low frequency interannual changes in the T–S relationship have been shown to occur on large spatial scales [*Picaut et al.*, 1989; *Delcroix et al.*, 1993; *Ando and McPhaden*, 1997]. Errors due to T–S variability might be correlated between adjacent stations used in the geostrophic calculation, and therefore be partially reduced when computing spatial density gradients.

Since the Ekman and geostrophic errors should be independent, the zonal net transport estimates (after the application of the 5–month running–mean) should be accurate to within $\epsilon_{total} = \sqrt{(1\text{Sv})^2 + (9\text{Sv})^2} \approx$ 9 Sv and the meridional net monthly transport accuracy (after the application of the 5–month running–mean) should be $\epsilon_{total} = \sqrt{(7\text{Sv})^2 + (2\text{Sv})^2} \approx$ 7 Sv. The time series mean net transport estimates should be accurate to within 3 Sv for the zonal transports and 2 Sv for the meridional transports.

A final test of the zonal net transport accuracies was undertaken by comparing 21 snapshot transport estimates made by hull–mounted acoustic Doppler current profilers (ADCP), provided by Gregory Johnson [personal communication, 1999, see also Johnson et al. 1999], to the transport time series at each of the eight corresponding TAO mooring lines coincident in time and space with the sections. The results indicated an RMS difference of 11 Sv and a mean difference of 3 Sv. These values compare well with the theoretical error estimates derived above considering the ADCP sections are near-synoptic while the transports calculated using our methods represent monthly averages.

The errors in the residual estimations of vertical cross–isotherm transports are a combination of the errors of the horizontal transports and the WWV. Since the errors in the WWV, geostrophic transports, and Ekman transports are independent, the estimated error bars for the vertical transport are given by the square–root of the sum of the squares of the component errors. For the full region of our study this yields error bars of 17 Sv for the values after the application of the 5–month running–mean and 5 Sv for the long–term mean. For the western and eastern subregions (Fig. 15) the estimated errors in the vertical transport across the 20°C isotherm are 15 Sv and 5 Sv for 5–month running–means and long–term means, respectively.

Acknowledgments

References

Ando, K. and M. J. McPhaden, Variability of surface layer hydrography in the tropical Pacific Ocean, *J. Geophys. Res.*, 102(C10), 23063–23078, 1997.

Battisti, D. S., Dynamics and thermodynamics of a warming event in a coupled tropical atmosphere–ocean model, *J. Atmos. Sci.*, 45(20), 2889–2919, 1988.

Bjerknes, J., A possible response of the atmospheric Hadley circulation to equatorial anomalies of ocean temperature, *Tellus*, 18, 820–829, 1966.

Bjerknes, J., Atmospheric teleconnections from the equatorial Pacific, *Mon. Wea. Rev.*, 97, 163–172, 1969.

Boulanger, J.-P. and C. Menkes, Long equatorial wave reflection in the Pacific Ocean from TOPEX/POSEIDON data during the 1992–1998 period, *Climate Dyn.*, 15(3), 205–226, 1999.

Brady, E. C., Interannual variability of meridional heat transport in a numerical model of the upper equatorial Pacific ocean, *J. Phys. Oceanogr.*, 24, 2675–2694, 1994.

Brady, E. C. and P. R. Gent, The seasonal cycle of meridional heat transport in a numerical model of the Pacific equatorial upwelling zone, *J. Phys. Oceanogr.*, 24, 2658–2673, 1994.

Bryden, H. L. and E. C. Brady, Diagnostic model of the three–dimensional circulation in the upper equatorial Pacific ocean, *J. Phys. Oceanogr.*, 15(10), 1255–1273, 1985.

Busalacchi, A. J., M. J. McPhaden, and J. Picaut, Variability in equatorial Pacific sea surface topography during the verification phase of the TOPEX/POSEIDON mission, *J. Geophys. Res.*, 99(C12), 24725–24738, 1994.

Cane, M. A., S. E. Zebiak, and S. C. Dolan, Experimental forecasts of El Niño, *Nature*, 321, 827–832, 1986.

Cronin, M. F. and M. J. McPhaden, Upper ocean salinity balance in the western equatorial Pacific, *J. Geophys. Res.*, 103, 27567–27587, 1998.

da Silva, A. M., C. C. Young, and S. Levitus, Atlas of surface marine data 1994, volume 1.: Algorithms and procedures, Technical Report 6, U.S. Department of Commerce, NOAA, NESDIS, Washington, D. C., 1994.

Davis, R. E., Preliminary results from directly measuring middepth circulation in the tropical and South Pacific, *J. Geophys. Res.*, 103(C11), 24619–24639, 1998.

Delcroix, T., G. Eldin, M. J. McPhaden, and A. Morliere, Effects of westerly wind bursts upon the western equatorial Pacific ocean, February–April 1991, *J. Geophys. Res.*, 98, 16379–16386, 1993.

Donguy, J.-R., A. Dessier, and Y. du Penhoat, Heat content displacement in the Pacific during the 1982-1983 El Niño event, *Oceanol. acta*, 12(3), 149–157, 1989.

Emery, W. J. and R. E. Thomson, *Data Analysis Methods in Physical Oceanography*. Pergamon Press, 1997.

Firing, E., Deep zonal currents in the central equatorial Pacific, *J. Mar. Res.*, 45(4), 791–812, 1987.

Fofonoff, N. P. and R. C. Millard. Algorithms for computation of fundamental properties of seawater. Unesco Technical Papers in Marine Science, No. 44, 53 pp., 1983.

Jin, F.-F., An equatorial ocean recharge paradigm for ENSO. part I: Conceptual model, *J. Atmos. Sci.*, 54(4), 811–829, 1997.

Jin, F.-F., An equatorial ocean recharge paradigm for ENSO. part II: A stripped–down coupled model, *J. Atmos. Sci.*, 54(4), 830–847, 1997.

Jin, F.-F. and S.-I. An, Thermocline and zonal advective feedbacks within the equatorial ocean recharge oscillator model for enso, *Geophys. Res. Let.*, 26(19), 2989–2992, 1999.

Johns, E., D. R. Watts, and H. T. Rossby, A test of geostrophy in the Gulf Stream, *J. Geophys. Res.*, 94(C3), 3211–3222, 1989.

Johnson, G. C. and M. J. McPhaden, Interior pycnocline flow from the subtropical to the equatorial Pacific Ocean, *J. Phys. Oceanogr.*, 29, 3073–3089, 1999.

Johnson, G. C., M. J. McPhaden, G. D. Rowe, and K. E. McTaggart, Upper equatorial Pacific Ocean current and salinity variability during the 1996–1998 El Niño–La Niña cycle, *J. Geophys. Res.*, 105(C1), 1037–1053, 2000.

Kessler, W. S., Observations of long Rossby waves in the northern tropical Pacific, *J. Geophys. Res.*, 95, 5183–5217, 1990.

Kessler, W. S. and B. A. Taft, Dynamic heights and zonal geostrophic transports in the central tropical Pacific during 1979–84, *J. Phys. Oceanogr.*, 17(1), 97–122, 1987.

McPhaden, M. J., Continuously stratified models of the steady-state equatorial ocean, *J. Phys. Oceanogr.*, 11(3), 337–354, 1981.

McPhaden, M. J., Genesis and evolution of the 1997–1998 El Niño, *Science*, 283, 950–954, 1999.

McPhaden, M. J. and X. Yu, Equatorial waves and the 1997-98 El Niño, *Geophys. Res. Let.*, 26(19), 2961–2964, 1999.

McPhaden, M. J., A. J. Busalacchi, R. Cheney, J.-R. Donguy, K. S. Gage, D. Halpern, M. Ji, P. Julian, G. Meyers, G. T. Mitchum, P. P. Niller, J. Picaut, R. W. Reynolds, N. Smith, and K. Takeuchi, The Tropical Ocean Global Atmosphere (TOGA) observing system: A decade of progress, *J. Geophys. Res.*, 103, 14169–14240, 1998.

Meinen, C. S. and M. J. McPhaden, Observations of warm water volume changes in the equatorial Pacific and their relationship to El Niño and La Niña, *J. Climate*, in press, 2000.

Meinen, C. S. and D. R. Watts, Vertical structure and transport on a transect across the North Atlantic Current near 42°N: Time series and mean, *J. Geophys. Res.*, in press, 2000.

Menkes, C., J.-P. Boulanger, and A. J. Busalacchi, Evaluation of TOPEX and basin–wide Tropical Ocean and Global Atmosphere–Tropical Atmosphere Ocean sea surface topographies and derived geostrophic currents, *J. Geophys. Res.*, 100(C12), 25087–25099, 1996.

Pares-Sierra, A. F., M. Inoue, and J. J. O'Brien, Estimates of oceanic horizontal heat transport in the tropical pacific, *J. Geophys. Res.*, 90(C2), 3293–3303, 1985.

Picaut, J. and R. Tournier, Monitoring the 1979-1985 equatorial pacific current transports with expendable bathythermograph data, *J. Geophys. Res.*, 96, 3263–3277, 1991.

Picaut, J., S. P. Hayes, and M. J. McPhaden, Use of the geostrophic approximation to estimate time–varying zonal currents at the equator, *J. Geophys. Res.*, 94(C3), 3228–3236, 1989.

Pond, S. and G. L. Pickard, *Introductory Dynamical Oceanography*. Pergamon Press, 2nd edition, 1983.

Reverdin, G., C. Frankignoul, E. Kestenare, and M. J. McPhaden, Seasonal variability in the surface currents of the equatorial Pacific, *J. Geophys. Res.*, 99(C10), 20323–20344, 1994.

Reynolds, R. W., A real–time global sea surface temperature analysis, *J. Climate*, 1, 75–86, 1988.

Reynolds, R. W. and D. C. Marsico, An improved real–time global sea surface temperature analysis, *J. Climate*, 6, 114–119, 1993.

Reynolds, R. W. and T. M. Smith, Improved global sea surface temperature analyses using optimum interpolation, *J. Climate*, 7, 929–948, 1994.

Reynolds, R. W. and T. M. Smith, A high resolution global sea surface temperature climatology, *J. Climate*, 8, 1571–1583, 1995.

Schopf, P. S. and M. J. Suarez, Vacillations in a coupled ocean–atmosphere model, *J. Atmos. Sci.*, 45, 549–566, 1988.

Sirven, J., C. Frankignoul, S. Février, N. Sennéchael, and F. Bonjean, Two-layer model simulations using observation and model-based wind stresses of the 1985-1992 thermocline depth anomalies in the tropical Pacific, *J. Geophys. Res.*, 103(C10), 21367–21383, 1998.

Smith, N. R., The BMRC ocean thermal analysis system, *Aust. Met. Mag.*, 44, 93–110, 1995.

Smith, N. R., An improved system for tropical ocean sub–surface temperature analyses, *J. Atmos. Oceanic Technol.*, 12, 850–870, 1995.

Smith, N. R. and G. Meyers, An evaluation of expendable bathythermograph and Tropical Atmosphere–Ocean Array data for monitoring tropical ocean variability, *J. Geophys. Res.*, 101(C12), 28489–28501, 1996.

Springer, S. R., M. J. McPhaden, and A. J. Busalacchi, Oceanic heat content variability in the tropical Pacific during the 1982-1983 El Niño, *J. Geophys. Res.*, 95(C12), 22089–22101, 1990.

Sun, D.-Z. and K. E. Trenberth, Coordinated heat removal from the equatorial Pacific during the 1986-87 El Niño, *Geophys. Res. Let.*, 25(14), 2659–2662, 1998.

Trenberth, K. E., The definition of El Niño, *Bull. Amer. Meteor. Soc.*, 78(12), 2771–2777, 1997.

Wang, W. and M. J. McPhaden, The surface layer heat balance in the equatorial Pacific Ocean, Part II: Interannual variability., *J. Phys. Oceanogr.*, in press, 2000.

Weisberg, R. H. and C. Wang, Slow variability in the equatorial west–central Pacific in relation to ENSO, *J. Climate*, 10, 1998–2017, 1997.

Wyrtki, K., El Niño–the dynamic response of the equatorial Pacific ocean to atmospheric forcing, *J. Phys. Oceanogr.*, 5, 572–584, 1975.

Wyrtki, K., Water displacements in the Pacific and the genesis of El Nino cycles, *J. Geophys. Res.*, 90(C4), 7129–7132, 1985.

Wyrtki, K. and J. Wenzel, Possible gyre-gyre interaction in the Pacific Ocean, *Nature*, 309, 538–540, 1984.

Zebiak, S. E., Oceanic heat content variability and El Niño cycles, *J. Phys. Oceanogr.*, 19, 475–486, 1989.

C. S. Meinen and M. J. McPhaden, NOAA/Pacific Marine Environmental Laboratory, 7600 Sand Point Way NE, OCRD/Building 3, Seattle, WA 98115. (e-mail: meinen@pmel.noaa.gov)

Received _____

Table 1. Mean transports of warm water ($T \geq 20°$C) into and out of the dashed region in Fig. 1, with positive indicating either north or east as appropriate, over January 1993–May 1999. Numbers in parentheses are a combination of the measurement accuracy and the standard error of the mean (see Appendix). Transports are in Sverdrups (1 Sv = 10^6 m^3 s^{-1}).

Section	Ekman transport			Geostrophic	Net transport		
	FSU	ECMWF	SCAT	transport	FSU	ECMWF	SCAT
8°N	+19 (2)	+23 (2)	+22 (3)	-6 (1)	+13 (2)	+17 (2)	+16 (2)
8°S	-25 (2)	-24 (2)	-25 (2)	+18 (4)	-7 (4)	-7 (4)	-8 (4)
156°E	-1 (1)	-0 (1)	-1 (1)	+16 (4)	+15 (4)	+16 (4)	+15 (4)
95°W	-0 (1)	-0 (1)	-0 (1)	-7 (4)	-7 (4)	-7 (4)	-7 (3)

Table 2. Statistics for the observed warm water volume change within the dashed region in Fig. 1 and the total net (Ekman plus geostrophic) transport of warm water across the four sides of the box. Ekman components were calculated using the wind product noted. Geostrophic components are identical for the three net transports.

Quantity	Comparisons of net transport to volume changes		
	Mean value	Standard Deviation	Correlation with obs. volume change
Observed volume change	-1 Sv	11 Sv	1.00
Total transport (FSU winds)	+2 Sv	11 Sv	0.52
Total transport (ECMWF winds)	-1 Sv	10 Sv	0.51
Total transport (SCAT winds)	-1 Sv	14 Sv	0.45

Table 3. Differences between total horizontal transport of warm water into the dashed region in Fig. 1, using the indicated wind products for the Ekman component and the observed changes in the warm water volume within the region. Geostrophic components are identical for the three comparisons. Negative mean imbalance would be balanced by downwelling across 20°C, positive would be balanced by upwelling.

Wind Product used for Ekman transports	Differences between net transport and volume changes	
	Mean imbalance	STD imbalance
FSU	-3 Sv	11 Sv
ECMWF	0 Sv	10 Sv
SCAT	0 Sv	13 Sv

Figure 1. Upper panel: Locations of the TAO array with ATLAS buoys (diamonds) and current meter moorings sites (squares). Dashed region indicates our study area. Lower panel: Locations of CTD profiles (small dots) taken during the 1990s and obtained from the NOAA/PMEL CTD database. Shaded areas indicate land.

Figure 2. Upper panel: Smoothed grid of specific volume anomaly, δ, as a function of pressure and Q_{500}. Developed using hydrography within 6°N–10°N and spanning the Pacific between 128°E and the coast of the Americas. Only casts reaching at least 1000 dbar were used. Contour level is 50×10^{-8} m^3 kg^{-1}. Lower panel: RMS scatter between δ directly calculated from CTD measurements and δ from the smoothed field, binned into 50 dbar by 5×10^{-8} J m^{-2} boxes. Contour levels are 10×10^{-8} m^3 kg^{-1} (solid contours) and 2×10^{-8} m^3 kg^{-1} (dotted contours). Higher values of Q_{500}, on left of plots, generally occur to the west.

Figure 3. Statistics for the 20°C isotherm depth, Z_{20}, over the years 1993–1999. Mean calculated over only 1993–1996 to avoid aliasing of the 1997–1998 El Niño into the mean structure. Standard deviation and empirical orthogonal functions (EOFs) determined over 1993–1999 after seasonal variations (defined as mean monthly differences from the long–term average, compute over 1993–1996) have been removed and 5–month running mean has been applied. Dashed contours in EOF structure indicate negative values. All contour values are in meters. Note different contour levels for plots. First and second EOF modes explain 45% and 35% of the total variance, respectively.

Figure 4. Time series of the warm ($T \geq 20°C$) water volume (solid line) within the dashed region in Fig. 1. The accuracy of the calculated WWV is about 0.015×10^{15} m^3 (see Appendix). Also shown is the mean sea–surface temperature (SST) anomaly (dashed line) averaged over the NINO3 region, which is bounded by 150°W–90°W, 5°S–5°N. Seasonal variations (defined as mean monthly differences from the long–term average, computed over 1993–1996) have been removed and 5–month running mean has been applied.

Figure 5. Statistics for the zonal component of the geostrophic velocity, U_g, at the surface over the years 1993–1999. Mean calculated over only 1993–1996 to avoid aliasing of the 1997–1998 El Niño into the mean structure. Standard deviation and empirical orthogonal functions (EOFs) determined over 1993–1999 after seasonal variations (defined as mean monthly differences from the long–term average, computed over 1993–1996) have been removed and 5–month running mean has been applied. Dashed contours in EOF structure indicate negative values. All contour values are in meters per second. Note different contour levels for plots. First and second EOF modes explain 49% and 13% of the total variance, respectively.

Figure 6. Geostrophic transport of warm water ($T \geq 20°C$) across 156°E, 155°W, and 95°W. Transport integrated between 8°S and 8°N. Positive transport is to the east. Transports are in Sverdrups (1 Sv = 10^6 m^3 s^{-1}). Seasonal variations (defined as mean monthly differences from the long–term average, computed over 1993–1996) have been removed and 5–month running mean has been applied.

Figure 7. Geostrophic transport of warm water ($T \geq 20°C$) across 8°N (solid line) and 8°S (dashed line). Transport integrated between 156°E and 95°W. Positive transport is to the north. Transports are in Sverdrups (1 Sv = 10^6 m^3 s^{-1}). Seasonal variations (defined as mean monthly differences from the long–term average, computed over 1993–1996) have been removed and 5–month running mean has been applied.

Figure 8. Ekman transport across 8°N (upper panel), and 8°S (lower panel). Transport integrated between 156°E and 95°W. Positive transport is to the north. Transports are in Sverdrups (1 Sv = 10^6 m^3 s^{-1}). Wind product used is indicated in legend. Seasonal variations (defined as mean monthly differences from the long–term average, computed over 1993–1996) have been removed and 5–month running mean has been applied.

Figure 9. Net (Ekman + geostrophic) transport across 8°N (solid line) and 8°S (dashed line). Transport integrated between 156°E and 95°W. Positive transport is to the north. ECMWF winds are used for the Ekman component. Transports are in Sverdrups (1 Sv = 10^6 m^3 s^{-1}). Seasonal variations (defined as mean monthly differences from the long–term average, computed over 1993–1996) have been removed and 5–month running mean has been applied.

Figure 10. Net (Ekman + geostrophic) transports across 156°E and 95°W. Upper panel shows total transports. Seasonal variations (defined as mean monthly differences from the long–term average, computed over 1993–1996) have been removed and 5–month running mean has been applied. Lower panel shows anomalies with 1993–1996 mean also removed. ECMWF winds are used for the Ekman component. Positive transport is to the east. Transports are in Sverdrups (1 Sv = 10^6 m^3 s^{-1}).

Figure 11. Net meridional transport (Ekman + geostrophic) across 8°N as a function of longitude and time. Units are Sv per degree longitude. Upper left panel shows the total transport, with seasonal variations (defined as mean monthly differences from the long–term average, computed over 1993–1996) removed and 5–month running mean applied. ECMWF winds are used for the Ekman component. Upper right panel shows the anomalous transports with the 1993–1996 mean also removed. Bold line indicates zero contour, dashed contours are negative. Positive transport is northward. Lower left panel shows temporal average transport over 1993–1996, lower right panel indicates temporal standard deviation over 1993–1999.

Figure 12. Same as for Fig. 11 but for transport across 8°S.

Figure 13. Comparison of total net transport into the region of interest (dashed lines) and the rate of change of warm water volume within the same region (temporal derivative of bold line in upper panel of Fig. 4). Upper panel shows comparison where the FSU wind product was used to obtain the Ekman components, middle panel utilized the ECMWF wind product, and the bottom panel used the SCAT wind product. Geostrophic components were the same for all panels. Transports are in Sverdrups ($1\,\mathrm{Sv} = 10^6\,\mathrm{m}^3\,\mathrm{s}^{-1}$). Seasonal variations (defined as mean monthly differences from the long–term average, computed over 1993–1996) have been removed and 5–month running mean has been applied.
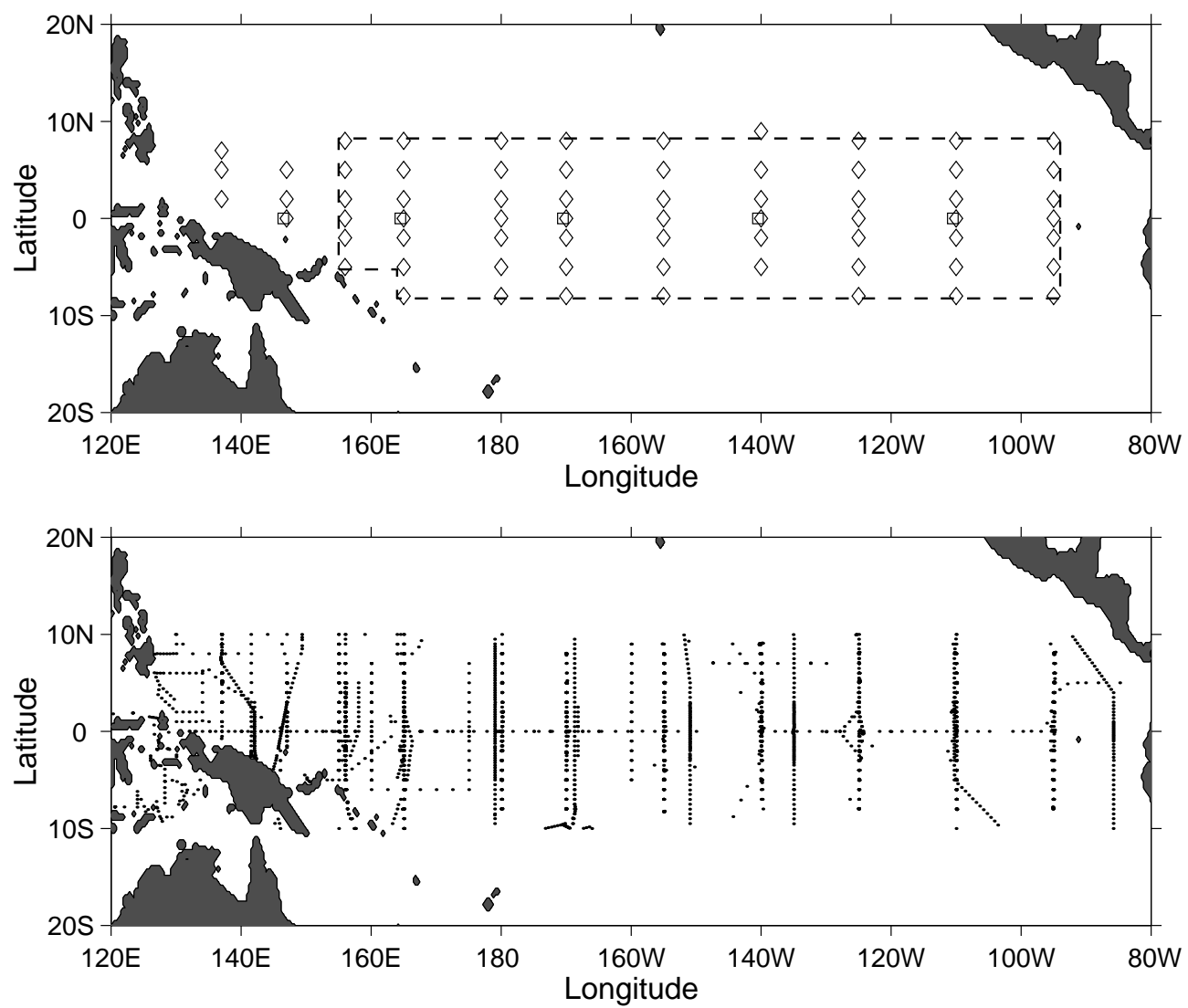
Figure 14. Upper panel–Warm water volume integrated within the region in Fig. 1 and split into parts west (solid line) and east (dashed line) of 155°W; Middle panel–Rate of change of warm water volume west of 155°W (bold line) along with the zonal convergence between 156°E and 155°W (dash–dot line) and the meridional convergence between 8°S and 8°N west of 155°W (dashed line); Lower panel–Rate of change of warm water volume east of 155°W (bold line) along with the zonal convergence between 155°W and 95°W (dash–dot line) and the meridional convergence between 8°S and 8°N east of 155°W (dashed line). Seasonal variations (defined as mean monthly differences from the long–term average, computed over 1993–1996) have been removed and 5–month running mean has been applied.

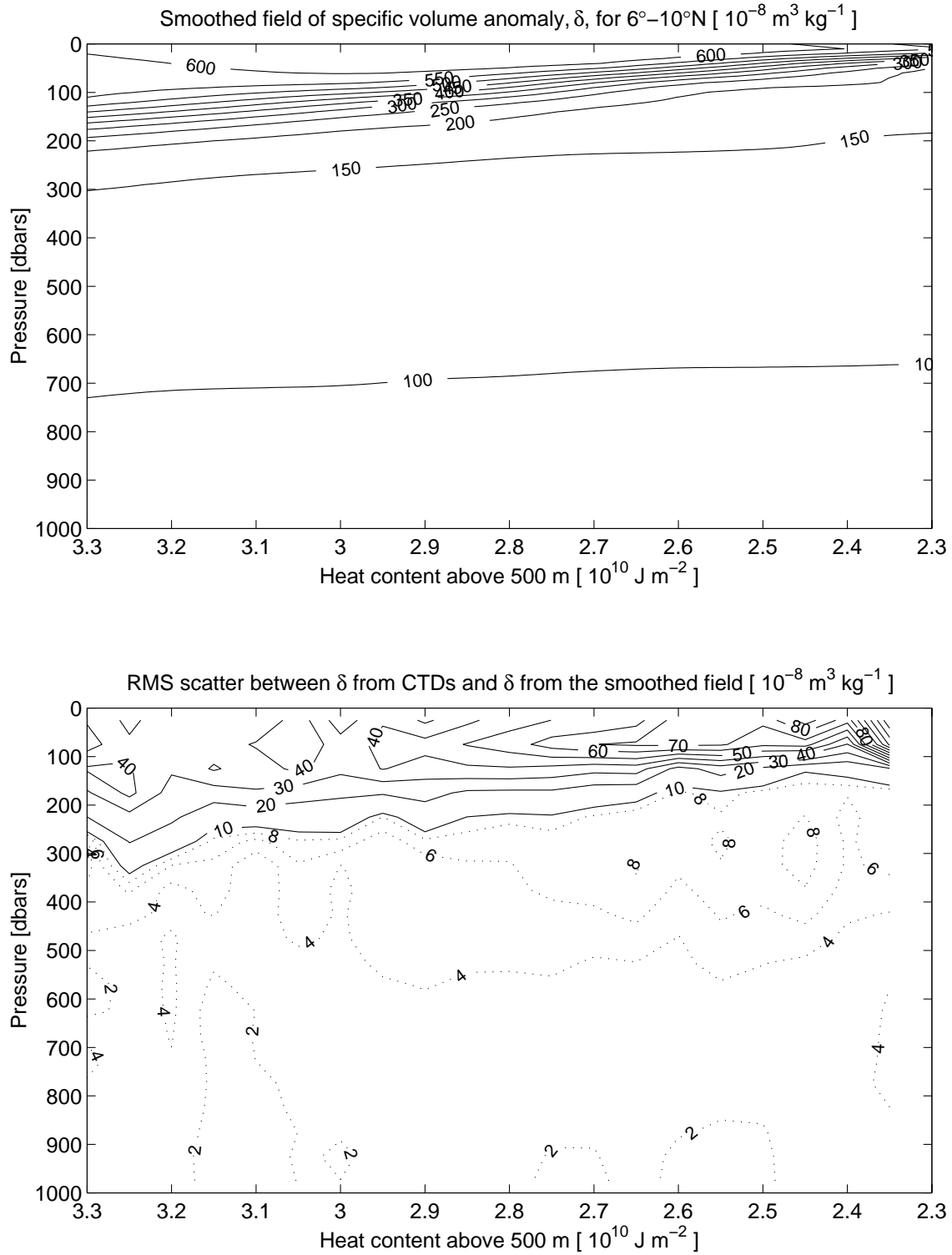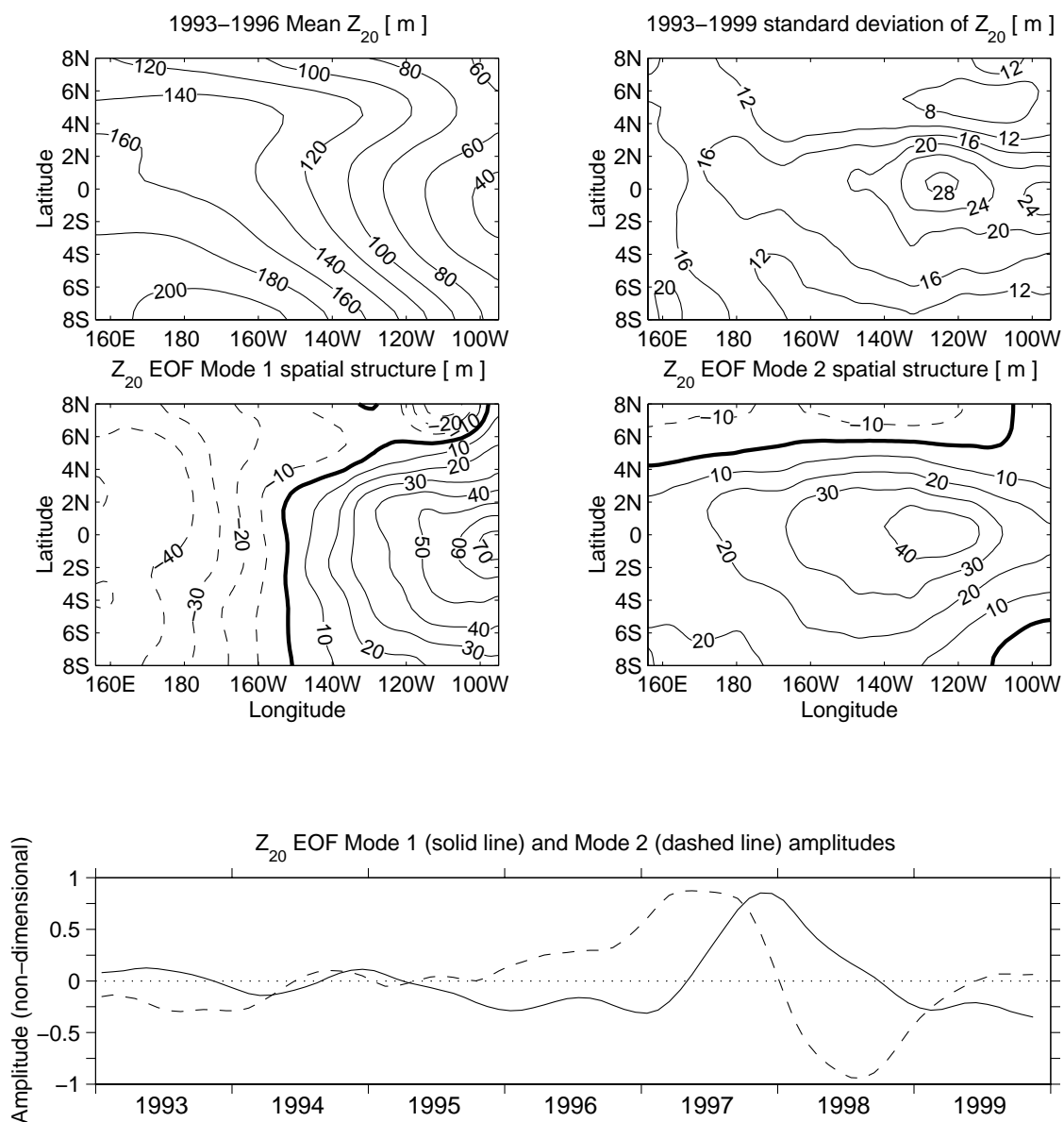**Figure 15.** Upper panel–Vertical volume transport across the 20°C isotherm within 8°S–8°N, 156°E–155°W (solid line), determined as the observed warm water volume changes minus the net transport through the four sides, and the zonal wind stress (ECMWF wind product) averaged over the same area (dashed line). Lower panel–Same as upper panel except for within 8°S–8°N, 155°W–95°W. Seasonal variations (defined as mean monthly differences from the long–term average, computed over 1993–1996) have been removed and 5–month running mean has been applied.

Figure 1.

Figure 2.

Smoothed field of specific volume anomaly, δ, for 6°–10°N [10^{-8} m^3 kg^{-1}]

RMS scatter between δ from CTDs and δ from the smoothed field [10^{-8} m^3 kg^{-1}]

Figure 3.

1993–1996 Mean Z_{20} [m]

1993–1999 standard deviation of Z_{20} [m]

Z_{20} EOF Mode 1 spatial structure [m]

Z_{20} EOF Mode 2 spatial structure [m]

Z_{20} EOF Mode 1 (solid line) and Mode 2 (dashed line) amplitudes

Figure 4.

Figure 5.

1993–1996 Mean U_g [m s^{-1}]

1993–1999 standard deviation of U_g [m s^{-1}]

U_g EOF Mode 1 spatial structure [m s^{-1}]

U_g EOF Mode 2 spatial structure [m s^{-1}]

U_g EOF Mode 1 (solid line) and Mode 2 (dashed line) amplitudes

Figure 6.

Figure 7.

Figure 8.
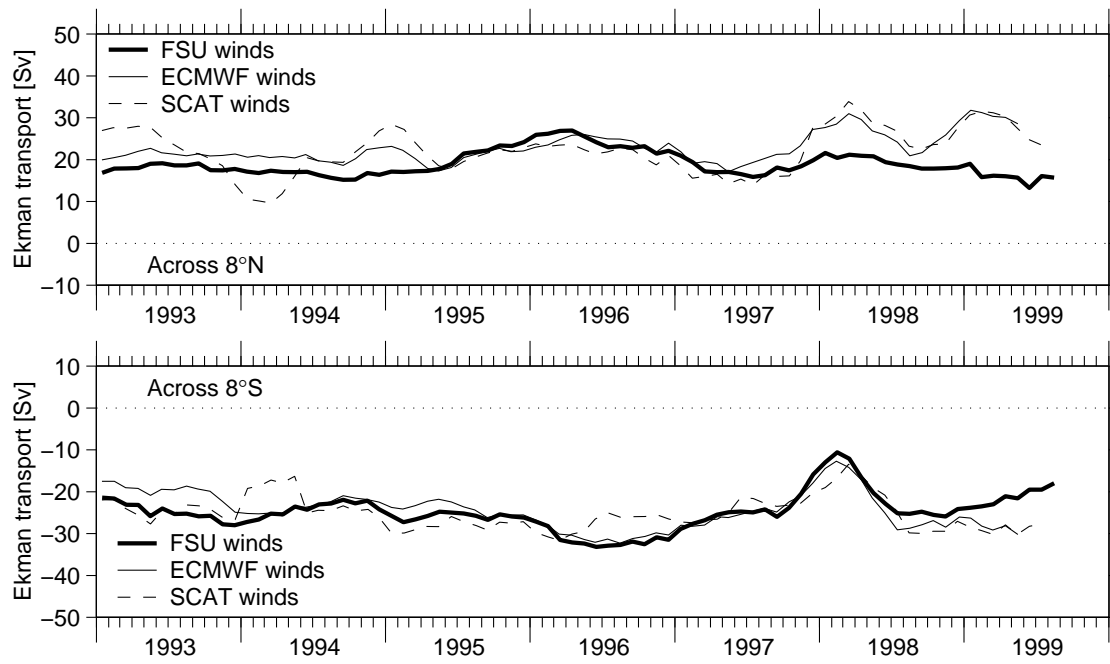
Figure 9.

Figure 10.

Figure 11.

Meridional transport across 8°N [Sv °Lon⁻¹]

Anomalous meridional transport across 8°N [Sv °Lon⁻¹]

Temporal mean transport [Sv °Lon⁻¹]

Transport standard deviation [Sv °Lon⁻¹]

Figure 12.

Meridional transport across 8°S [Sv °Lon^{-1}]

Anomalous meridional transport across 8°S [Sv °Lon^{-1}]

Temporal mean transport [Sv °Lon^{-1}]

Transport standard deviation [Sv °Lon^{-1}]
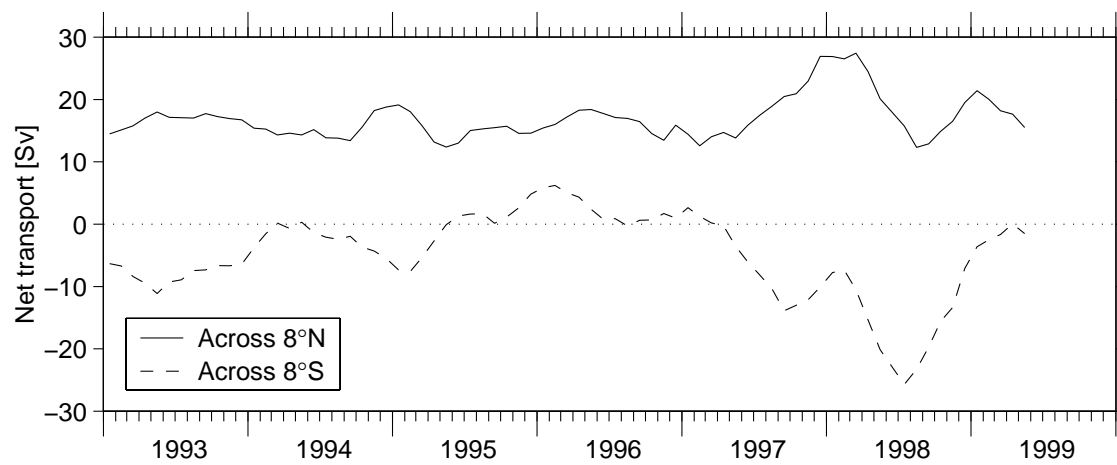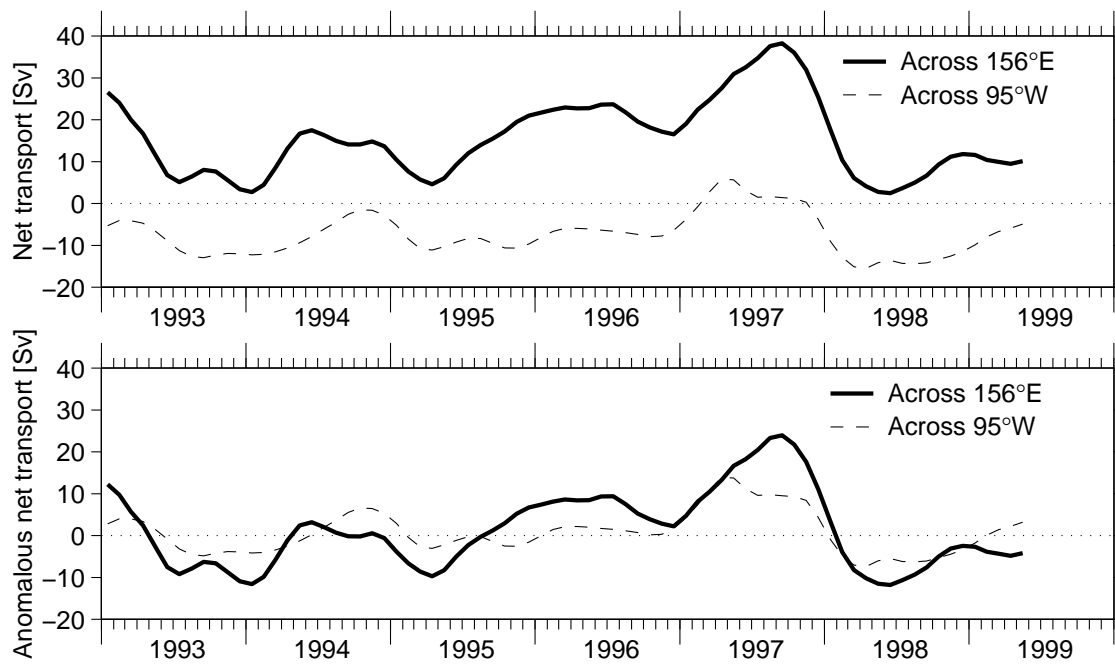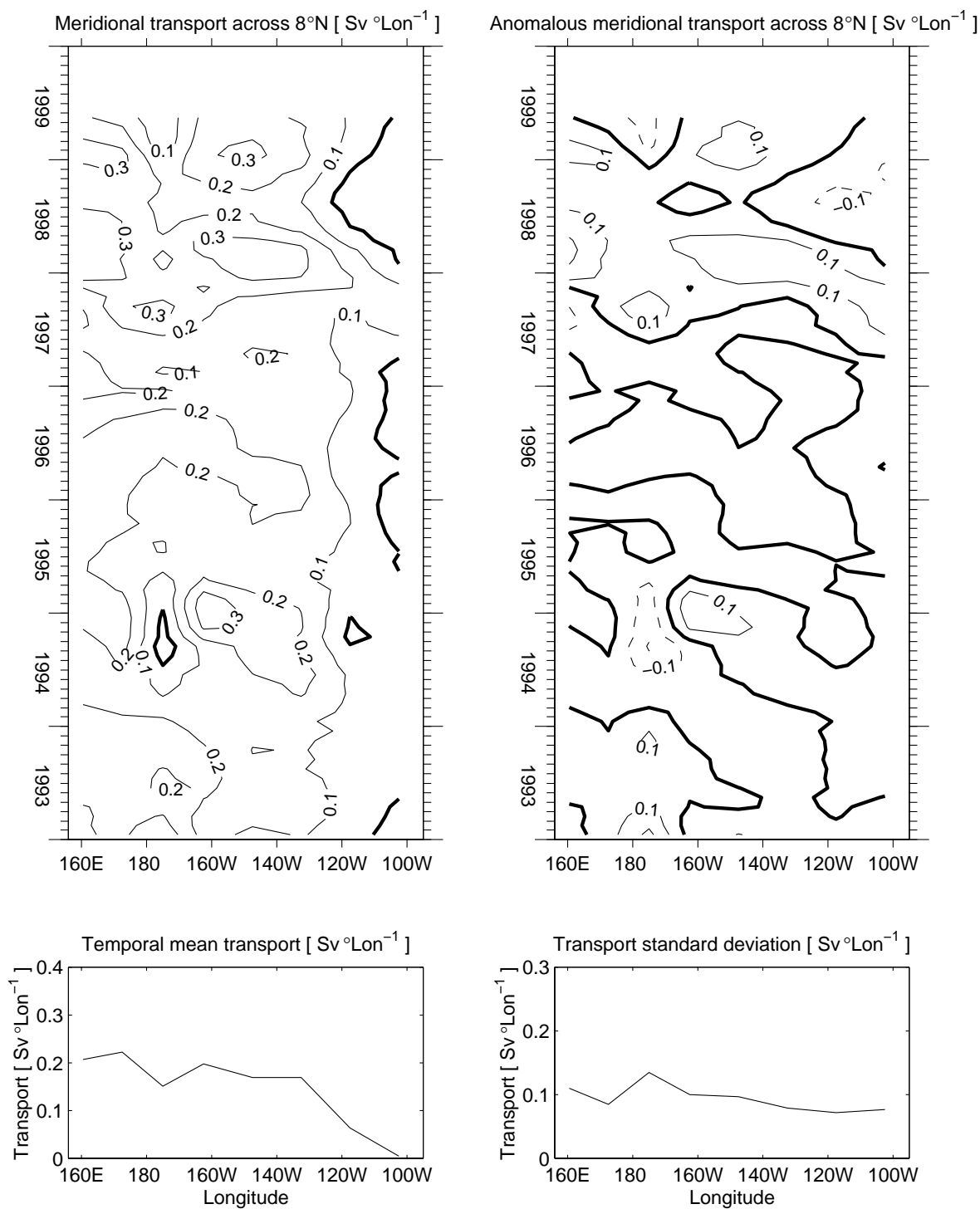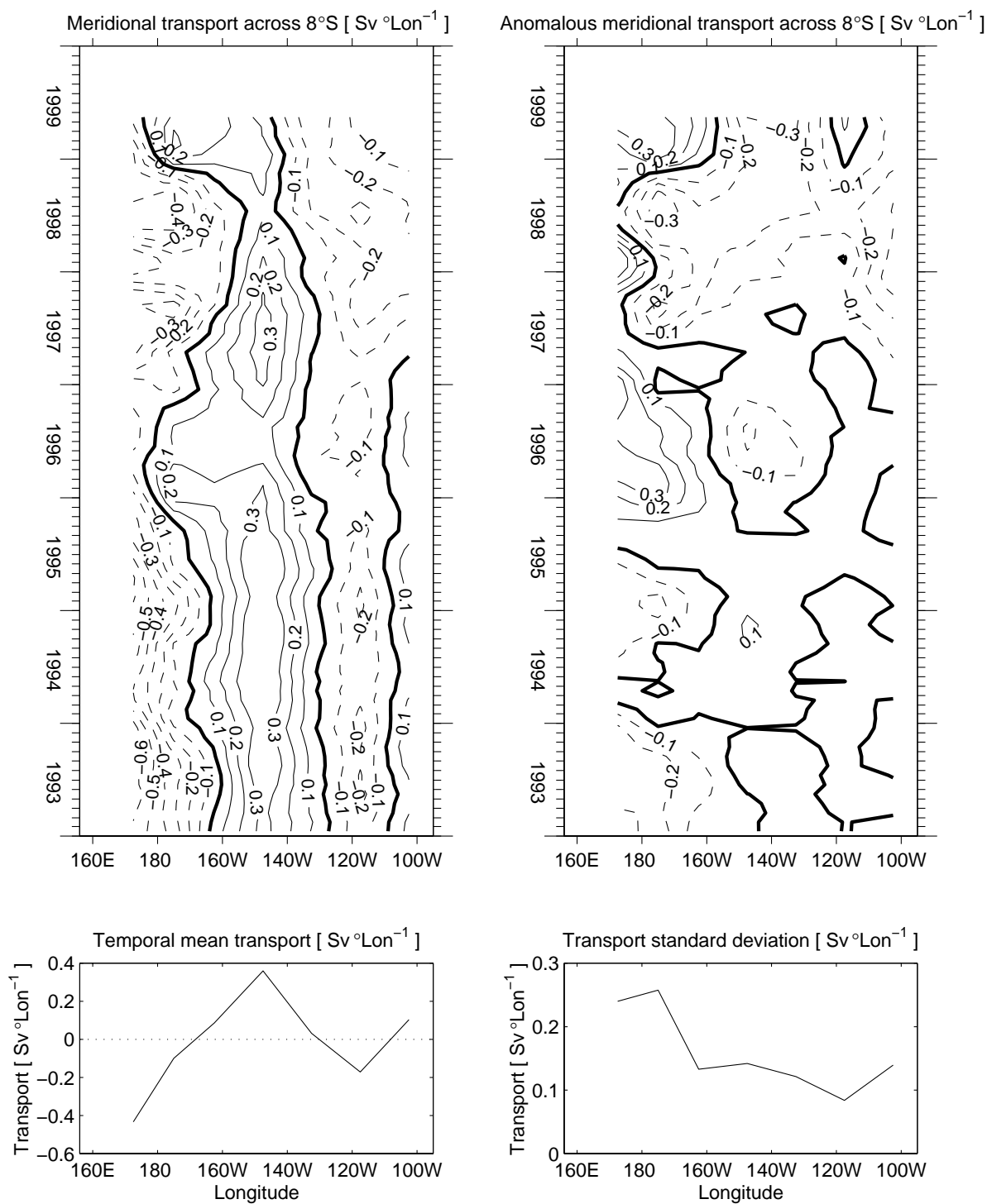
Figure 13.

Figure 14.

Figure 15.